250-GeV/c π^-p multiplicity distributions and the two-component model

P. J. Hays, R. N. Diamond, R. K. Clark, S. Hagopian, and J. E. Lannutti

Florida State University, Tallahassee, Florida 32306

J. P. Berge, D. Bogert, R. Hanft, R. Harris,* F. R. Huson, S. Kahn,[†] and W. Smart

Fermi National Accelerator Laboratory, Batavia, Illinois 60510

(Received 11 February 1980)

The charged-particle multiplicity distribution from 250-GeV/c π^-p interactions in the Fermilab 15-ft bubble chamber is presented. The corrections to the raw data are described. Fits to these data along with other high-energy bubble-chamber data show that cluster models with two components—a low-multiplicity, diffractive component and a high-multiplicity, nondiffractive component—describe the data fairly well. The charged multiplicity of each cluster is found to be ~ 2, while the number of clusters for each component grows linearly with $\ln(s)$. The multiplicity moments are consistent with other experiments. We find $\langle n_c \rangle = 8.427 \pm 0.059$, $f_2^{cc} = 8.66 \pm 0.11$, $\langle n_c \rangle/D = 2.038 \pm 0.023$. The total inelastic cross section is $\sigma_I = 21.42 \pm 0.50$ mb.

I. INTRODUCTION

Multiplicity distributions from high-energy interactions have been extensively studied in bubble-chamber experiments. The primary emphasis of these experiments has been on the charged-particle multiplicities because of the low detection efficiency for neutral particles. Many theoretical models have been introduced to account for these charged-particle multiplicity distributions.[1]

This paper presents the final results on charged-particle multiplicities from an exposure of the hydrogen-filled 15-ft bubble chamber at Fermilab to a 250-GeV/c π^- beam. The early motivation for this exposure was to study neutral-strange-particle production. These results have been published previously.[2] The models which describe charged-particle production also make predictions about neutral-particle production and future publications will present our results on that subject.

We wish to emphasize that the results presented here are based primarily on scan information. There is of course much to be learned about charged-particle momentum correlations, but the measurements necessary for this have so far not been carried out. We therefore rely on some results from an earlier 205-GeV/c π^-p exposure of the Fermilab 30-in. bubble chamber,[3] as well as some of our measurements made in connection with neutral-strange-particle production[2] and γ-ray production.[4]

II. EXPERIMENTAL DETAILS

We discuss here the beam, bubble chamber, scan rules, and film statistics.

A. Beam

300-GeV/c protons were extracted from the Fermilab Synchrotron and directed onto a 30-cm-long Cu target. Negative particles produced at an angle of 1 mr with an energy of 250 GeV/c and a 0.1% momentum bite were selected for our beam.

A kicker magnet located upstream of the chamber was used to limit high-flux pulses and resulted in an average of approximately 4 particles/pulse at the entrance of the bubble chamber. The beam profile at the chamber entrance was 10 cm in the vertical direction and 60 cm in the horizontal direction.

We assume a beam contamination the same as that obtained by the 205-GeV/c collaboration[3] since the same target, production angle, and momentum bite were used in both experiments. The K^- contamination is $(1.4 \pm 0.2)\%$ and the μ^- contamination $(2.6 \pm 0.5)\%$, while the small $\bar{p}$ contamination is ignored.

B. Chamber

The 15-ft Fermilab bubble chamber is a 12-ft chamber with a 3-ft nose cone added at the beam entrance to increase the path length for hadron physics. It is inside a superconducting magnet which has a maximum magnetic field of 30 kG but which was run at 21 kG for our experiment. The liquid-hydrogen density was found from density-temperature and temperature-vapor pressure curves to be $\rho = 0.0635 \pm 0.0006$ g/cm^3.

C. Scanning

60% of the film was scanned at Florida State University and 40% at Fermilab using MicroMetrics machines with 15× magnification and 60× magnification, respectively. The FSU tables were modified to allow selection of 25× or 60× magnification in certain views for better resolution of congested events.

In the scan a square grid with each zone corre-

20

sponding to approximately 16 cm in the chamber was used for locating interactions and defining the fiducial volume. The fiducial volume for primary vertices was chosen to be 281 ± 2 cm long with no cut perpendicular to the beam direction, while all neutral-particle vertices beyond the nose cone were accepted during the scan.

Information recorded for each frame included the number of beam tracks, the location and number of prongs of all primary and secondary interactions (within ~80 cm of the primary vertex), stopping and identifiable nonstopping protons, Dalitz pairs, kinks (charge and location), and $\pi\mu e$'s.

Information recorded for neutral-particle vertices included their location, and classification as G (at least one identified $e^{\pm}$ and zero opening angle), V (nonzero opening angle, or identifiable hadron as evidenced by ionization or interacting secondary track), A (ambiguous between G or V), or N star (more than two tracks). The G's and A's were essentially equal in number and subsequent measurements found that essentially all the G's were γ conversions, while 90% of the V's and 10% of the A's were neutral-strange-particle decays. Since 95% of the G's and A's combined are γ conversions, for convenience hereafter they will be referred to as γ's.

In order for a frame to be considered acceptable it was required to have no more than 15 beam tracks and to have at least two good views. As this was an engineering run for the chamber, approximately 20% of the film had to be rejected on these grounds.

In Table I we show the overall statistics for this experiment. Based on a total interaction path length of $(2.62 \pm 0.04) \times 10^7$ cm, and making cor-

TABLE I. Film statistics.

Total frames	40 337
Good frames	31 770
Beam tracks	109 884
Events	22 330
G's	12 565
A's	12 545
V's	2 505
Microbarn equivalent	1.00 ± 0.02
Number of events with	
$G + A = 0$	9 617
$G + A = 1$	5 936
$G + A \geq 2$	6 777

rections for a beam contamination at $(-4.0 \pm 0.7)\%$ and a beam attenuation of $(-12.2 \pm 1.4)\%$, and using a hydrogen density of 0.0635 ± 0.0006 g/cm^3 and total a cross section of 24.60 ± 0.05 mb,[5] we obtain a microbarn equivalent of 1.00 ± 0.02 events/μb.

A double scan was performed on 15% of the film with any discrepancies resolved by a third (conflict) scan. In Table II we show the results obtained for the identification efficiencies ϵ_I, the probability that a vertex was classified correctly, and finding efficiencies ϵ_F, the probability of finding a vertex for primary interactions and γ's (G's and A's combined), under the assumption that the conflict scan was perfect. The identification efficiency is taken to be $\epsilon_I = N_{13}/N_1$ where N_1 is the number of events found in scan 1 and N_{13} the number of correctly identified events in scan 1 as determined by the conflict scan 3. The finding efficiency is essentially N_{13}/N_3. The 6% misidentifi-

TABLE II. Scan efficiencies ϵ_I = identification efficiency (probability that a vertex was correctly identified). ϵ_F = finding efficiency. Angular brackets indicate an average over all remaining data.

		(a) Primary vertices			
	Prongs	$\gamma = 0$	$\gamma = 1$	$\gamma = 2$	$\gamma \geq 3$
ϵ_I	all		$\langle 0.943 \pm 0.004 \rangle$		
ϵ_F	2	0.69 ± 0.02	0.85 ± 0.04	0.74 ± 0.08	0.72 ± 0.12
	4–10		$\langle 0.919 \pm 0.005 \rangle$		
	12	0.90 ± 0.03	0.91 ± 0.03	0.99 ± 0.01	0.97 ± 0.01
	≥ 14		$\langle 0.919 \pm 0.005 \rangle$		

		(b) γ vertices		
	Prongs	$\gamma = 1$	$\gamma = 2$	$\gamma \geq 3$
ϵ_I	2–4		$\langle 0.881 \pm 0.005 \rangle$	
	6	0.92 ± 0.02	0.92 ± 0.02	0.83 ± 0.03
	≥ 8		$\langle 0.881 \pm 0.005 \rangle$	
ϵ_F	2	$0.76 \pm .05$	$0.67 \pm .07$	$0.90 \pm .05$
	≥ 4		$\langle 0.767 \pm 0.006 \rangle$	

cation of primary interactions ($\epsilon_I = 0.94$) arises generally from secondary interactions being mislabeled as beam interactions and vice versa, while the 12% misidentification of GA's is due mainly to G's being confused with V's or secondary interactions and vice versa. These efficiencies depend to some extent on the number of γ rays associated with a primary vertex and this must be taken into account when corrections are made to the raw scan data.

III. CORRECTIONS

In order to obtain the partial cross sections in Table III a number of corrections to the raw data must be made.

Short-recoil protons

A significant fraction of the production of low-multiplicity events (< 8 prongs) is attributable to diffractive processes.[6] In beam diffraction the target proton may recoil with low momentum and in target diffraction the decay proton from the diffractive state may also have momentum sufficiently low (less than 140 MeV/c) that it will not be visible to the scanners. Since the diffractive effects predominate at low multiplicity we have taken all 1-, 3-, 5-, and 7-prong events to be 2-, 4-, 6-, and 8-prong events, respectively, in which a recoil proton was not observed.

The number of such low-multiplicity odd-prong events is consistent with the number expected from the t distributions measured at 205 GeV/c.[3] For the 205-GeV/c data severe scanning losses were noted for $|t| < 0.03$ (GeV/c)^2 whereas for our data losses occur for $|t| < 0.06$ (GeV/c)^2. This is presumably due to larger bubble size and greater demagnification onto the film.

Unresolved secondary interactions

Since interactions of charged secondaries should be even pronged, unresolved secondary interactions result in an apparent odd-prong primary topology. Table IV gives the multiplicity distribution of resolved secondary interactions. The correction for unseen secondary interactions which result in odd-prong primary topologies is given by

$$N_i = N_i^0 + \alpha_2 N_{i+1}^0 + \alpha_4 N_{i+3}^0 + \alpha_6 N_{i+5}^0 ,$$

where N_i is the corrected number of primary interactions with i prongs; N_i^0 is the observed number of primary interactions with i prongs; $\alpha_k = 0.66$, 0.21, and 0.13 are the probabilities for producing 2-, 4-, or 6-prong secondary interactions, respectively. The α_k were obtained from Table IV under the assumption that the ≥ 9-prong secondary

interactions, of which 95% have undetermined multiplicity, are distributed in the same ratio as the < 8-prong secondary interactions.

Hidden γ-ray conversions

γ rays which predominantly result from π^0 decay convert into $e^+ e^-$ pairs with an average conversion length of $L_c = 1466 \pm 30$ cm. Those γ-ray conversions near the primary vertex whose electrons cannot be identified as such are often confused with the true secondary tracks and hence a correction must be made for hidden γ rays. Low-momentum electrons from the pair are readily identified.

The number of γ-ray conversions N found in an interval between x and $x + dx$ is given by

$$N(x)dx = \left[\int_0^x P(x') \frac{\epsilon_F(x')}{\epsilon_I(x')} \langle \gamma \rangle e^{-x''L_c} \frac{dx'}{L_c} \right] dx ,$$

where $P(x)$ is the number of primary vertices per unit length, $\langle \gamma \rangle$ is the average number of γ rays per event, ϵ_F is the γ-ray scanning efficiency, and ϵ_I is a correction for γ rays which turn out to be unassociated with the primary vertex. In order to determine the number of missing γ rays close to the primary vertex we find the average values of the ϵ factors at intermediate distances from the primary vertex and extrapolate the number,

$$\int_x^{x+\Delta x} N(x')dx' ,$$

of γ rays in a bin of width Δx from moderate x to $x = 0$ cm. Figure 1(a) shows

$$\alpha(x) = \frac{\epsilon_F^{(x)}}{\epsilon_I(x)} \langle \gamma \rangle ,$$

while Fig. 1(b) shows $\int_x^{x+\Delta x} N(x')dx'$. From this figure we estimate that 1225 ± 147 γ rays are missing and presumably confused with tracks from the primary events. The multiplicity distribution is corrected by reducing by two the primary event multiplicity, the distribution of these events being proportional to the average number of γ rays actually found for each topology greater than 4 prongs. The 2-prong events require no correction while the 4-prong correction is 3.9% compared to 4.9% for the higher-multiplicity events.

Hidden neutral strange particles

Neutral strange particles which decay near the primary vertex may be confused with the charged secondaries. To correct for these missing strange particles, we use a sample of 1000 three-constraint events plot in Fig. 2 the "linearized lifetime," $Q(l)$, defined by

TABLE III. Scan statistics, corrections, and partial cross sections.

Number of prongs	(a) Raw no. of events	(b) Short-proton correction	(c) Secondary interactions	(d) Hidden γ's	(e) Dalitz pairs	(f) Hidden V's (strange)	(g) Net corrections	(h)[a] Final no. of events	(i) Cross section (mb)
0	13				+7±3		7±3	21±5	0.02±0.01
1		−6							
2 elastic								3200±100	3.20±0.10
2 inelastic	2547	+6±2		+81±10	+12±3	+52±7	151±13	1475±140	1.47±0.14
3		−68							
4	3037	+68±8	+14±4	+103±11	+12±3	+10±3	+207±15	3328±79	3.32±0.10
5		−47							
6	3682	+47±7	+38±7	+54±8	+8±3	+3±2	+150±13	3931±88	3.92±0.12
7		−67							
8	3878	+67±8	+112±12 / −106	−20±5	−4±2	−12±4	+143±16	4127±92	4.12±0.12
9									
10	3230		+124±12 / −120	−45±7	−8±3	−16±4	+55±15	3371±80	3.36±0.10
11									
12	2022		+125±12 / −130	−60±8	−10±3	−15±4	+40±15	2310±61	2.31±0.08
13									
14	1340		+114±12 / −131	−51±8	−8±3	−10±3	+45±15	1422±60	1.42±0.06
15									
16	714		+81±9 / −91	−30±6	−5±2	−6±2	+40±11	744±38	0.77±0.04
17									
18	338		+59±8 / −68	−15±4	−2±2	−3±2	+39±10	386±25	0.39±0.03
19									
20	153		+42±7 / −51	−11±4	−2±2	−2±1	+27±8	185±17	0.18±0.02
21									
22	56		+22±5 / −25	−2±1			+20±5	78±11	0.078±0.011
23									
24	34		+18±4 / −26	−5±2	−1±1	−1±1	+11±5	47±9	0.047±0.009
25									
26	6		+2±1 / −2				+2±1	8±3	0.008±0.003
27									
28	3		+2±1 / −3				+2±1	5±2	0.005±0.002
29									
30	1							1±1	0.001±0.001
Total inelastic	19536							22417±261	21.42±0.50

[a] Includes primary scan efficiencies and 2-prong corrections.
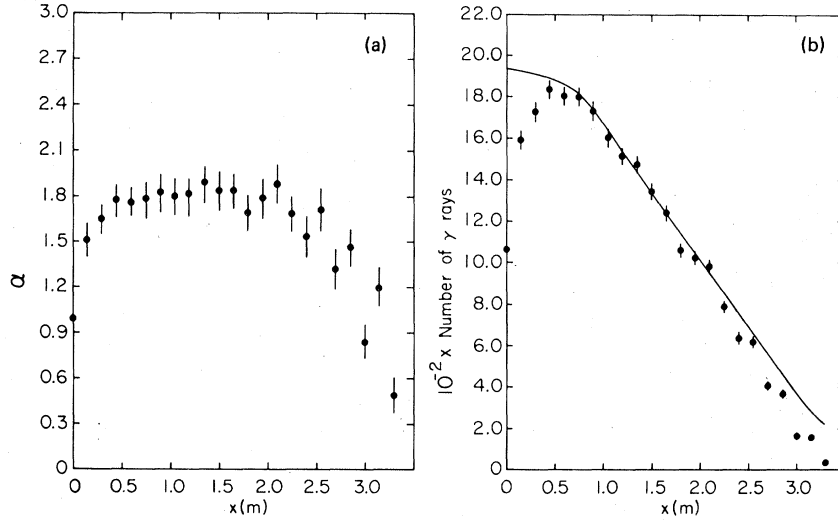
FIG. 1. (a) $\alpha(x)$, the ratio of finding efficiency to identification efficiency (see text for definitions), is plotted as a function of position in the bubble chamber. (b) The number of γ rays found as a function of position in the bubble chamber. The curve is the expected distribution based on the primary event distribution and the value of $\alpha(x)$ found at intermediate distances.

$$Q(l) = \frac{\int_0^l e^{-x/\beta\gamma c\tau} dx}{\int_0^{l_{max}} e^{-x/\beta\gamma c\tau} dx},$$

where $\beta\gamma c\tau$ is the relativistic decay length and l_{max} the maximum path length for a given event. This plot should be flat, but we note that for $Q(l)$ less than 0.2 there is a loss of 116 ± 14 decays, which for the entire exposure corresponds to 313 ± 48 decays.[7] For a maximum available path length of 350 cm, $Q(l) < 0.2$ implies that the losses occur for $l < 7.5$ cm.

Unrecognized Dalitz pairs

Based on the number of γ-ray conversions found during the scan and our estimates of the scanning efficiencies, the 955 Dalitz pairs ($\gamma e^+ e^-$ decay modes of the π^0) represent a loss of $(17.2 \pm 0.5)\%$

from the number expected. This does not mean that our scanners had an 83% efficiency for finding Dalitz pairs, but rather that they could not distinguish between them and close γ conversions. Since the effect on the multiplicity distribution is the same for both processes, we have made no attempt to identify the true Dalitz pairs.

TABLE IV. Prong multiplicities of resolved interacting secondaries (even-pronged primary events only).

Prongs	No. of interacting secondaries
0	132
1	2
2	1681
3	10
4	530
5	2
6	338
7	0
8	42
≥ 9	282
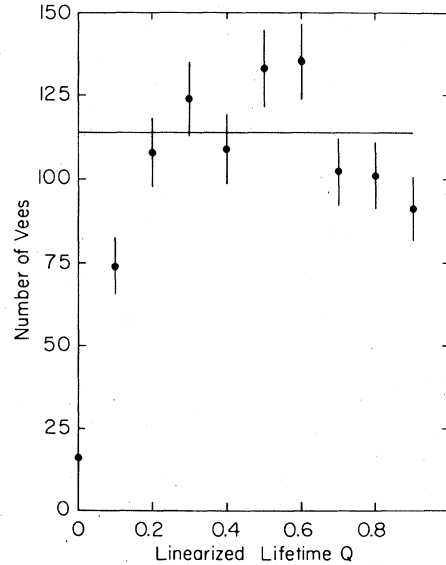
FIG. 2. Linearized lifetime Q for neutral-strange particles. The distribution should be flat, but falls at large Q because of fiducial-volume losses and falls at low Q because of scanning losses.

2-prong events

The 2-prong events must be treated separately from the rest of the data because the scanning efficiency is considerably different and depends on the momentum of the recoil proton. The problem is one of recognition; if the recoil proton is not noticed, the event will be missed because of the small laboratory scattering angle.

The 2-prong cross section is composed of elastic and inelastic events. To estimate the elastic contribution to our scanned data we assume an elastic cross section of 3.2 mb (Ref. 8) and a differential cross section of the form

$$\frac{d\sigma_{el}}{dt} = A e^{bt},$$

with $A = 27.4$ mb/(GeV/c^2)^2 and $b = 8.8$ (GeV/c^2)$^{-2}$ (Ref. 3). The 205-GeV/c $\pi^- p$ collaboration noted a 50% drop in their double-scan efficiency for finding elastic events for $|t| < 0.03$ (GeV/c^2)^2. The losses in the present experiment are more severe due to poorer film quality, greater demagnification of the film, and the fact that our results come from only a single scan. We estimate our scanning efficiency for elastics with recoil proton momentum less than 240 MeV/c [$|t| < 0.06$ (GeV/c^2)^2] to be only 30% of the remaining 2-prong scanning efficiency.

Since 40% of the elastic cross section has $|t| < 0.06$ (GeV/c^2)^2 we estimate the number of missing elastic events for $|t| < 0.06$ (GeV/c^2)^2 to be

$$(1.0 - 0.3 \times 0.7) \times 0.4\sigma_{el}\mu = 1045 \pm 25.$$

In this equation the elastic cross section σ_{el} is 3.2 mb, μ, the microbarn equivalent, is 1.00 ± 0.02 events/μb for our experiment, and the elastic scanning efficiency is 70%.

The error in the inelastic 2-prong cross section can be only crudely estimated. Taking a 3% statistical error in the number of prongs found, a 4% uncertainty in the scanning efficiency, a 2% error in normalization, a 6% error in the elastic slope,[3] and a 20% error in the reduced 2-prong scanning efficiency in quadrature, we find an error of 10% for the inelastic 2-prong cross section. The 2-prong cross sections are

$$\sigma_{elastic} = 3.20 \pm 0.10 \text{ mb} \quad \text{(Ref. 8)}$$

and

$$\sigma_{inelastic} = 1.47 \pm 0.14 \text{ mb}.$$

IV. RESULTS

In Table III, column (i) we present the topological cross sections from the scan of our 250-GeV/c $\pi^- p$ film. The raw scan information is found in column (a). The odd-prong events with seven or fewer secondaries, column (b), move to the next higher even-prong topology and the higher-multiplicity odd-prong events are redistributed among the lower-multiplicity events as described in the previous section. The next correction, due to unresolved secondary interactions, is shown in column (c). Columns (d), (e), and (f) of Table III show, respectively, the net correction to the multiplicity distribution due to hidden γ-ray conversions, unrecognized Dalitz pairs, and hidden V's. The net corrections and corrected event totals for each multiplicity are given in columns (g) and (h). In order to obtain the final event numbers in column (h), the net correction of column (g) is added to the raw number of events in column (a) and then multiplied by the efficiency ratio ϵ_I/ϵ_F. The cross sections given in column (i) are obtained from the event total using the mb equivalent and scan efficiencies given in Tables I and II.

The moments of the multiplicity distribution shown in Table V are found to be in agreement with other $\pi^- p$ experiments.[12]

Comparison with other experiments

A great many theoretical models have been proposed in an attempt to understand the multiplicity distributions which arise in high-energy multiparticle production reactions. These models take two general forms: (1) models in which pions are produced independently according to some distribution function and (2) models in which the pions come from clusters which may possibly be identified with resonances and which in turn are produced according to their own distribution function. Included in category (1) are the "critical-fluid model" of Thomas[1] in which the multiplicity distribution is analogous to the number-density fluctuation of a one-dimensional fluid at the critical point and

TABLE V. Charged-particle-multiplicity moments. D = dispersion $\equiv \langle n^2 - \langle n \rangle^2 \rangle^{1/2}$. γ_1 = skew $\equiv \mu_3/\mu_2^{3/2}$ where $\mu_K = \langle (n - \langle n \rangle)^K \rangle$ is the Kth central moment. γ_2 = kurtosis $\equiv \mu_4/\mu_2^2 - 3$. $d_q = \langle n_{ch}^q \rangle / \langle n_{ch} \rangle^q$.

$\langle n_{ch} \rangle = 8.427 \pm 0.059$	$d_2 = 1.240 \pm 0.005$
$\langle n_{ch}^2 \rangle = 88.1 \pm 1.0$	$d_3 = 1.804 \pm 0.020$
$\langle n_{ch}(n_{ch} - 1) \rangle = 79.68 \pm 0.98$	$d_4 = 2.977 \pm 0.057$
$D = 4.134 \pm 0.037$	$d_5 = 5.45 \pm 0.16$
$\langle n_{ch} \rangle / D = 2.038 \pm 0.023$	$d_6 = 10.91 \pm 0.44$
$\gamma_1 = 0.700 \pm 0.026$	$d_7 = 23.5 \pm 1.2$
$\gamma_2 = 0.505 \pm 0.086$	$d_8 = 54.2 \pm 3.6$
$f_2^{cc} = 8.66 \pm 0.11$	$d_9 = 132 \pm 11$

a "Gaussian model"[10] in which particles are produced according to a Gaussian distribution with an energy-dependent mean. Category (2) includes models in which pion-production results via the creation of jets or clusters of pions in various isospin configurations (see, for example, Berger *et al.*[1]). The results of our attempts to fit high-energy multiplicity distributions to a number of these models are shown below. We find that in general the cluster models [category (2)] work better than independent-particle-production models [category (1)] but that, in order for the cluster models to fit the high-energy data well, two different components must contribute to cluster production.

The inelastic topological cross sections for our data are plotted in Figs. 3 and 4. The curves in Fig. 3 are the predictions for five single-component models which are, cluster models with $\sigma(I=0)$, $\rho(I=1)$, or $\rho\rho(I=0)$ clusters,[9] a Gaussian model,[10] and a critical-fluid model.[11] The cluster models assume a Poisson distribution for the number of clusters. Only the critical-fluid model among the independent-particle-production models we have tried gives a good fit ($\chi^2 = 2.2/\text{DF}$). In Fig. 4 curves from four two-component cluster

models are shown. All these models give excellent fits to our data although some of the parameters for the ρ-$\rho\rho$ model must be constrained to physically sensible values. We only wish to point out with Figs. 3 and 4 that, although single-component cluster models have some difficulty fitting our data, two-component models fit easily. In order to distinguish between two-component cluster models we must investigate their energy dependence, comparing our results with other experiments.

For the purpose of examining the energy dependence of different models we have used the multiplicity distributions of π^-p experiments whose beam momenta ranged from 100 to 360 GeV/c and of pp experiments with beam momenta between 50 and 400 GeV/c.[12]

We have attempted to fit a two-critical-fluid model[13] to the π^-p data as well as to the pp data. The multiplicity distribution is given by

$$\sigma_{n_{\text{ch}}n_0} = Ae^{-y}\frac{g_0^{n_0}}{n_0!}\frac{g_{\text{ch}}^{n_{\text{ch}}}}{n_{\text{ch}}!}(y - nb)^n e^{an^2/y},$$

with the parameter a representing the long-range two-particle attraction, b the short-range repulsion, g the coupling constant, and y the rapidity range. The indices N_0 and N_{ch} are, respectively,
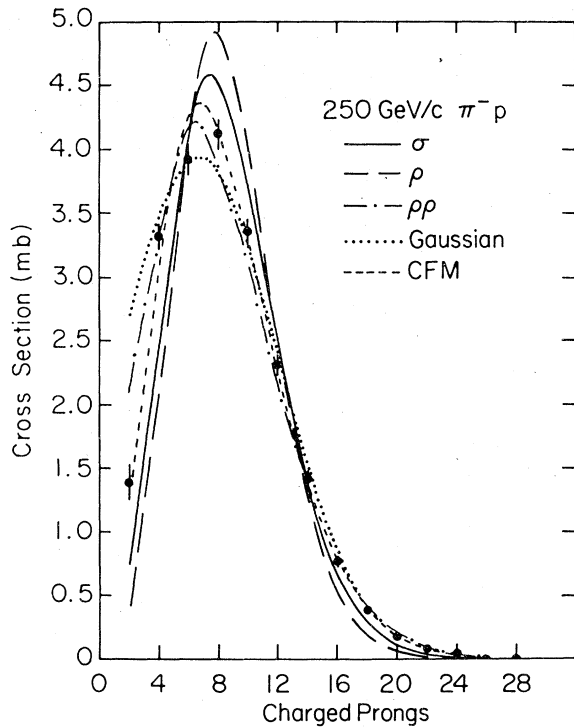
FIG. 3. The 250-GeV/c π^-p multiplicity data is plotted along with the fits from five models: a critical-fluid model (CFM), a Gaussian model and three single-component cluster models: σ, ρ, and $\rho\rho$.
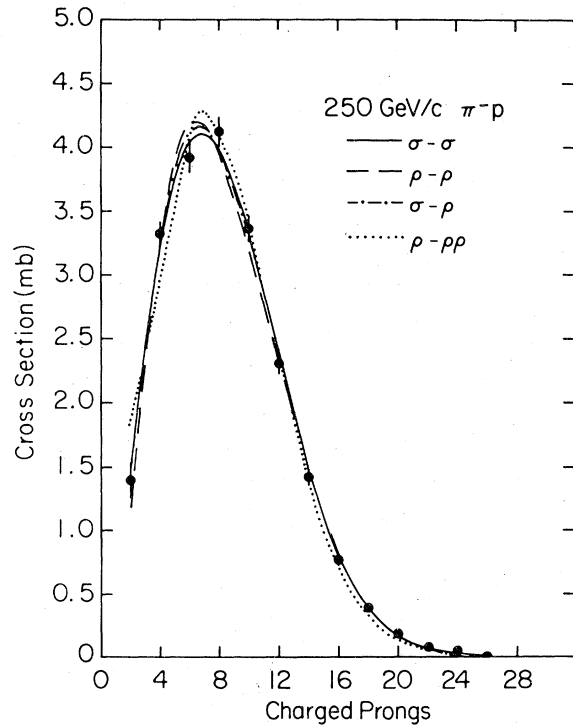
FIG. 4. The 250-GeV/c π^-p multiplicity data is plotted along with the fits from four two-component cluster models: σ-σ, ρ-ρ, ρ-σ, and ρ-$\rho\rho$.

the number of neutral and charged particles pro-
duced. Letting these parameters vary we find lit-
tle change from the van der Waals values $a = \frac{27}{64}$,
$b = \frac{1}{8}$, and $g_0 \equiv \frac{1}{2} g_{ch} \equiv \frac{1}{3} g = 0.232$. As evidenced by
the fits in Fig. 5 the critical-fluid model ($\chi^2 = 26/$
DF) does not display the correct energy depen-
dence. The width of the predicted multiplicity dis-
tributions does not grow rapidly enough with ener-
gy.

Single-component models with π, σ, ρ, or $\rho\rho$
clusters in which the mean number of clusters
grows logarithmically with energy do not fit the
data well. We choose not to present the plots of

these fits. We turn instead to two-component
models.

In Fig. 5 we have plotted the high-energy bubble-
chamber data and curves showing the fits obtained
for a number of two-component models, as well as
for the critical fluid model. A model with σ-like
diffractive and σ-like nondiffractive components
gives a good fit ($\chi^2 = 1.9/$DF) to the high-energy
data. In this model the mean number of clusters
in each component, the inelastic cross section,
and the diffractive fraction of the inelastic cross
section are all assumed to vary as $a + b \ln(s)$,
where s is the square of the overall c. m. energy.
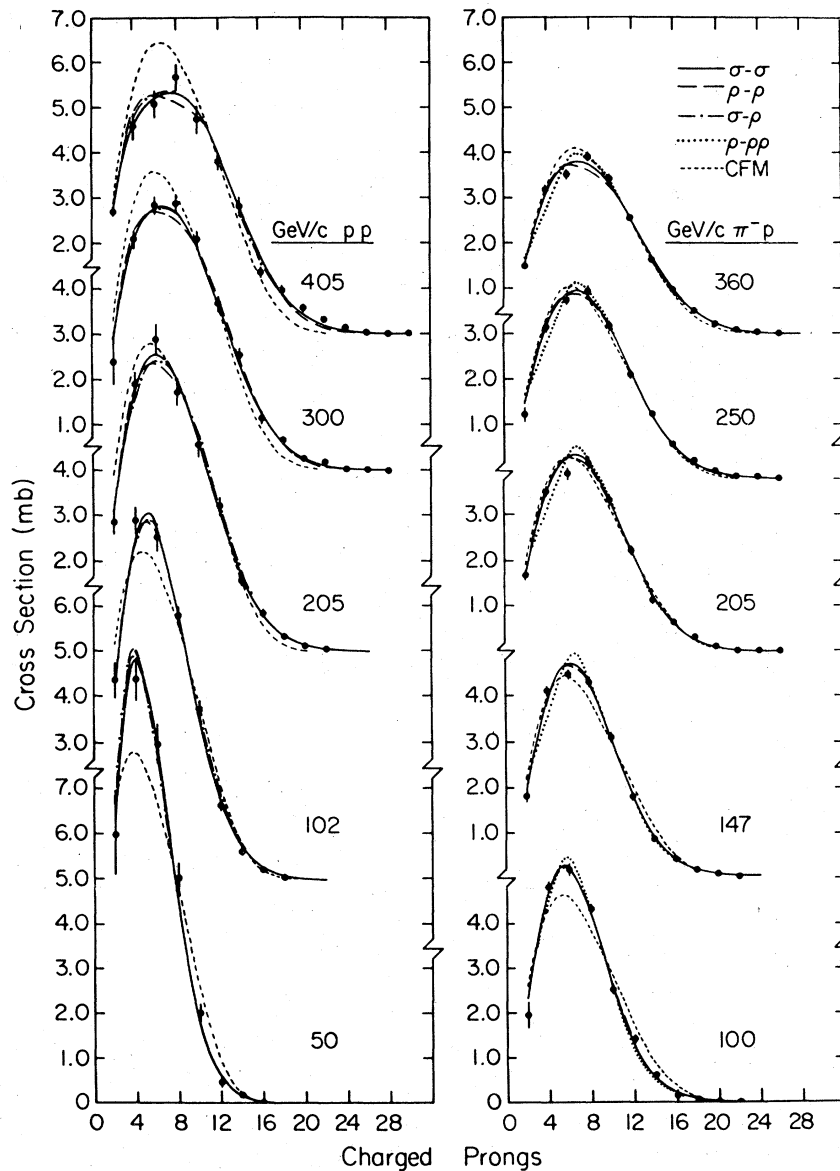
FIG. 5. The high-energy pp and π^-p multiplicity data is plotted along with the energy-dependent fits to the critical-
fluid model and four two-component cluster models: σ-σ, ρ-ρ, ρ-σ, and ρ-$\rho\rho$.

The values of the fit parameters are given in Table VI. The two-component (diffractive and nondiffractive) model of Harari[14] predicts a value of 0.5 for the ratio of the slopes of the diffractive and nondiffractive mean multiplicities, but as evidenced by the results in Table VI the two-component σ model does not support a value of 0.5 for the ratio. However, another prediction of Harari's two-component model, namely, that the diffractive partial cross sections, which are shown in Table VII, should approach constant values does appear to be born out by the fit.

The other two-component models are parametrized in a manner similar to the parametrization of the two-component σ model. The two-component model in which the clusters are ρ-like objects and whose cluster multiplicity is Poisson distributed about an energy-dependent mean also gives a reasonable fit to the data. The χ^2 is only marginally worse than for the two-component σ model. The largest contributions to the χ^2 come from the highest-energy experiments indicating that the cluster multiplicity tends to be greater than the $\langle n_c^c \rangle = 1.33$ for ρ-like clusters. The fit parameters for this ρ-ρ model are given in Table VI.

We have tried to fit the high-energy bubble-chamber data with a two-component model whose clusters are $I = 0$ pairs of ρ mesons. This two-component $\rho\rho$-$\rho\rho$ model whose parameters are given in Table VI is not plotted in Fig. 5 because it does not fit the data well ($\chi^2/DF = 4.6$). Presumably the mean charge multiplicity of each cluster ($\langle n_c^c \rangle = 2.67$) is too great. The fit to the higher-energy data is somewhat better than it is to the lower-energy data.

By combining either a σ-like or ρ-like diffractive component with a $I = 0$ $\rho\rho$-like nondiffractive component one would expect to fit the data reasonably well and in fact a χ^2 of ~ 2.0/DF is obtained. Table VI indicates, however, that the fitting program wants to reverse the roles of each component and make a ρ-like nondiffractive component and $\rho\rho$-like diffractive component. This runs counter to naive expectations.

V. CONCLUSION

We have measured the charged-particle multiplicity distributions in 250-GeV/c $\pi^- p$ interactions. A number of corrections had to be made to the raw data, corrections which because of the operating conditions of the Fermilab 15-ft bubble chamber and because of slightly poorer resolution are somewhat larger than in other high-energy bubble-chamber experiments. The data are consistent with the other experiments and together these data

TABLE VI. The mean number diffractive and nondiffractive clusters, the inelastic cross section, and relative amounts of diffractive and nondiffractive components are parametrized by the form $a + b \ln s$. Fit results for the $a + b \ln s$ parameters for various single-component and two-component models are presented.

Model	Mean number of diffractive clusters		Mean number of nondiffractive clusters		Inelastic cross section (mb)		Diffractive-component fraction of inelastic cross section		χ^2/DF
	a	b	a	b	a	b	a	b	
$\pi^- p\ \sigma\sigma$	-1.65 ± 0.03	0.505 ± 0.005	-4.18 ± 0.01	1.277 ± 0.003	19.1 ± 0.1	0.37 ± 0.02	-0.718 ± 0.007	0.156 ± 0.001	1.9
$pp\ \sigma\sigma$	1.32 ± 0.03	0.004 ± 0.005	-3.70 ± 0.01	1.195 ± 0.002	26.9 ± 0.2	0.87 ± 0.03	0.342 ± 0.007	-0.011 ± 0.001	1.8
$\pi^- p\ \rho\rho$	-0.26 ± 0.03	0.503 ± 0.004	-5.07 ± 0.02	1.873 ± 0.003	19.3 ± 0.1	0.33 ± 0.02	-0.015 ± 0.004	0.063 ± 0.007	2.6
$pp\ \rho\rho$	0.08 ± 0.03	0.400 ± 0.005	-5.00 ± 0.02	1.844 ± 0.004	28.0 ± 0.2	0.70 ± 0.03	0.328 ± 0.005	0.0071 ± 0.0009	1.9
$\pi^- p\ \rho\rho-\rho\rho$	-6.98 ± 0.56	2.130 ± 0.100	-1.94 ± 0.23	0.663 ± 0.040	19.8 ± 1.4	0.27 ± 0.23	2.390 ± 0.190	-0.340 ± 0.030	4.6
$pp\ \rho-\rho\rho$	-8.68 ± 0.17	2.460 ± 0.030	-2.97 ± 0.04	0.816 ± 0.007	26.4 ± 0.3	1.00 ± 0.92	2.060 ± 0.070	-0.290 ± 0.010	2.2

TABLE VII. Diffractive partial cross sections for the two-component σ model.

p_{lab} (GeV/c)	2 prongs	4 prongs	6 prongs	8 prongs	σ_D/σ_I
	π^-p partial cross sections (mb)
360	1.26	2.06	1.69	0.92	0.30
250	1.22	1.78	1.29	0.63	0.24
205	1.17	1.59	1.08	0.49	0.21
147	1.04	1.24	0.74	0.29	0.16
100	0.79	0.79	0.39	0.13	0.10
p_{lab} (GeV/c)	2 prongs	4 prongs	6 prongs	8 prongs	σ_D/σ_I
	pp partial cross sections (mb)
405	2.32	3.12	2.10	0.94	0.27
300	2.33	3.13	2.11	0.95	0.28
205	2.34	3.14	2.11	0.95	0.28
102	2.36	3.17	2.12	0.95	0.29
50	2.38	3.19	2.13	0.95	0.29

show that single-component models whose energy dependence is of the form $a + b \ln s$ do not fit well. Good fits are obtained with two-component models having a low-multiplicity (diffractive) component and a higher-multiplicity (nondiffractive) component. We obtain the best fit for cluster multiplicities of ~2 charged particles per cluster, in agreement with recent results from the CERN ISR (Ref. 15), where, in addition, it was found from studying the charged-particle rapidity correlations that the cluster mass is ~1.5 GeV/c^2.

ACKNOWLEDGMENTS

*Present address: Washington University, St. Louis, Missouri.

†Present address: Brookhaven National Laboratory, Upton, New York.

[1] E. L. Berger et al., Phys. Rev. D 7, 1412 (1973); J. Whitmore, Phys. Rep. 27, 187 (1976); G. H. Thomas, Phys. Rev. D 8, 3042 (1973); A. H. Mueller, ibid. 4, 150 (1971); O. Czyzewski and K. Rybicki, Nucl. Phys. B47, 633 (1972); D. Horn and A. Schwimmer, ibid. B52, 627 (1973); D. Drijard and S. Pokorski, Phys. Lett. 43B, 509 (1973); P. Grassberger and H. I. Miettinen, Nucl. Phys. B82, 26 (1974).

[2] D. Bogert et al., Phys. Rev. D 16, 2098 (1977).

[3] D. Ljung et al., Phys. Rev. D 15, 3163 (1977).

[4] Patrick J. Hays, Ph.D. thesis, Florida State University, 1980 (unpublished).

[5] A. S. Carroll et al., Phys. Lett. 61B, 303 (1976).

[6] For diffraction studies in π^-p interactions in our energy range see F. C. Winkelmann et al., Phys. Rev. Lett. 32, 121 (1974); J. W. Lämsä et al., Phys. Rev. D 18, 3933 (1978); for pp interactions see J. W. Chapman et al., Phys. Rev. Lett. 32, 257 (1974); F. T. Dao et al., Phys. Rev. Lett. 45B, 399 (1973); S. J. Barish et al., Phys. Rev. Lett. 31, 1080 (1973).

[7] 2505 vees were found in the scan and we assume that the fraction lost near the primary vertex is the same as for measured subsample for which a three-constraint fit to K_s^0, Λ, or $\bar{\Lambda}$ was successful. See Ref. 2.

[8] J. Whitmore, Phys. Rep 10C, 302 (1974).

[9] A. Arneodo and J. Kubar-Andre, Nucl. Phys. B77, 309 (1974); Lett. Nuovo Cimento 12, 1 (1975); D. Drijard and S. Pokorski, Phys. Lett. 43B, 509 (1973); E. L. Berger, D. Horn, and G. H. Thomas, Phys. Rev. D 7, 1412 (1973); D. Horn and A. Schwimmer, Nucl. Phys. B52, 627 (1973).

[10] G. D. Kaiser, Daresbury Nuclear Physics Laboratory Report No. DNPL/P148, 1973 (unpublished).

[11] R. C. Arnold and G. H. Thomas, ANL Report No. ANL/HEP 7257, 1972 (unpublished).

[12] Data on topological and total inelastic cross sections were obtained from pp interactions: (405 GeV/c) C. Bromberg et al., Phys. Rev. Lett. 31, 1563 (1973); (303 GeV/c) F. T. Dao et al., ibid. 29, 1627 (1972); (300 GeV/c) A. Firestone et al., Phys. Rev. D 10, 2080 (1974); (205 GeV/c) S. Barish et al., ibid. 9, 2689 (1974); (102 GeV/c) same as 405 GeV/c; (100 GeV/c) W. M. Morse et al., Phys. Rev. D 15, 66 (1977); (69 GeV/c) M. Boratav et al., Nucl. Phys. B111, 529 (1976); (60 GeV/c) C. Bromberg et al., Phys. Rev. D 15, 64 (1977); (50 GeV/c) V. V. Ammosov et al., Phys. Lett. 42B, 519 (1972); and from π^-p interactions: (360 GeV/c) A. Firestone et al., Phys. Rev. D 14, 2902 (1976); (205 GeV/c) D. Ljung et al., ibid. 15, 3163 (1977); (147 GeV/c) D. Fong et al., Nucl. Phys. B102, 386 (1976); (100 GeV/c) E. L. Berger et al., ibid. B77, 365 (1974).

[13] G. H. Thomas, Phys. Rev. D 8, 3042 (1973).

[14] H. Harari, in Phenomenology of Particles at High

Energies, proceedings of the Fourteenth Scottish Universities Summer School in Physics, 1973, edited by P. L. Crawford and R. Jennings (University of Glasgow, Scotland, 1974) p. 297.

[15]H. D. Wahl, in *Proceedings of the 19th International Conference on High Energy Physics, Tokyo, 1978*, edited by S. Homma, M. Kawaguchi, and H. Miyazawa (Phys. Soc. of Japan, Tokyo, 1979), p. 72.